Supporting Information for

A multimodal analytical toolkit to resolve correlated reaction pathways: The case of nanoparticle formation in zeolites

Daniel O'Nolan,†[a] Haiyan Zhao,†[b] Zhihengyu Chen,[a] Antonin Grenier,[a] Michelle L. Beauvais,[a] Mark A. Newton,[c] Tina M. Nenoff,*[d] Peter J. Chupasa,*[a,b,e] and Karena W. Chapman*[a,b]

CONTENTS

[a] *Department of Chemistry, Stony Brook University, 100 Nicolls Rd, Stony Brook, New York, 11790, United States. Email: Karena.Chapman@stonybrook.edu*
[b] *X-ray Science Division, Advanced Photon Source, Argonne National Laboratory, Lemont, Illinois, 60439, United States.*
[c] *Department of Chemistry and Applied Biosciences, ETH Zürich, Zürich, Switzerland.*
[d] *Sandia National Laboratories, Materials Chemicals and Physics Center, Albuquerque, New Mexico 87185, United States. Email: tmnenof@sandia.gov*
[e] *Associated Universities Inc, 16th Street NW, Suite 730, Washington, DC, 20036. Email: pchupas@aui.edu*
† These authors contributed equally.

EXPERIMENTAL DETAILS

Materials Preparation. Silver LTA zeolite ($Ag_{12}(AlO_2)_{12}(SiO_2)_{12}O_{48}{\cdot}27\ H_2O$; AgA, Si/Al = 1) was prepared *via* ion-exchange[1] of commercial zeolite A (Zeochem, Na-4A). Zeolite A (10 g) was mixed with 200 mL of 0.1 M $Ag(NO_3)$ and heated at 95 °C while stirring for 1 h. Upon cooling, the sample was filtered in air and washed ×3 with deionized water; the filtrate was confirmed to be free of silver ions. The final product was collected and placed in a 95 °C furnace for 4 h. The AgA sample was then cooled and stored, in a sealed vial, in a dark cabinet until characterization.

DRIAD-X measurements. Simultaneous X-ray, Infrared data was collected at beamline 11-ID-B of the Advanced Photon Source (APS) at Argonne National Laboratory. The AgA sample was loaded into the sample cup of a Harrick Instruments High Temperature Reaction Chamber, modified to allow simultaneous diffuse reflectance infrared and angular dispersive X-ray (DRIAD-X) measurements (**Figure S1**).[1] The sample environment was mounted to a Bruker Vertex 80 spectrometer within a Praying Mantis optic, modified to allow transmission of incident/scattering X-rays. The X-ray beam (0.2 mm (V) × 0.5 mm (H), λ = 0.1370 Å) was aligned to probe a sample volume just below the surface of the sample, coincident with the probe region of the IR beam. X-ray data was collected using an amorphous-Si Perkin-Elmer detector, with acquisition of a no-X-ray "dark frame" every 20 images.[2] Diffuse reflectance infrared Fourier transform spectroscopy (DRIFTS) spectra were collected in the range 7000–400 cm^{-1} with a spectral resolution of 2 cm^{-1} using a linearized, high sensitivity MCT (mercury, cadmium, telluride) detector.

Variable temperature X-ray total scattering and DRIFTS data were collected under inert (He) and reducing (4% H_2 in He) atmospheres, heating at a rate of *ca.* 3.5 °C min^{-1} to a maximum temperature of *ca.* 320 °C. X-ray and Infrared data acquisitions were initiated simultaneously prior to heating, with synchronized data collected at 1 min intervals. Sample surface temperature was calibrated with a second thermocouple touching the top surface of the sample.

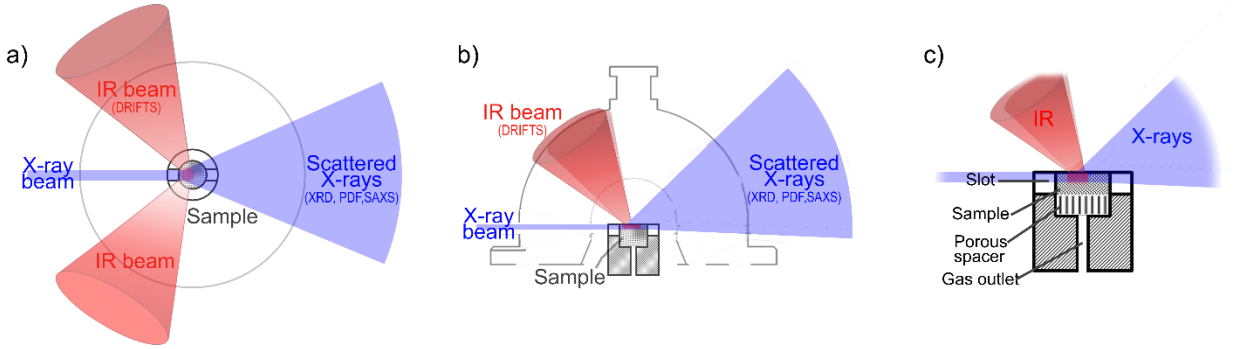

Figure S1. *Schematics of the DRIAD-X experimental geometry. The IR and X-ray beams probes a volume near the top of the sample. The gas flows through the sample cup from this top surface.*

Data reduction. The two-dimensional X-ray scattering images were reduced to one-dimensional data within Fit2D.[3] Data were normalized to the scattering intensity observed in the high-Q region to account for fluctuations in the incident beam. The detector geometry was calibrated based on a scattering image collected for KBr powder.

PEARSON CORRELATION ANALYSIS

The Pearson correlation coefficient (r) represents the linear relationship between two sets of data: r = 1, positive correlation (e.g. identical data); r = 0, no correlation (e.g. random data); r = −1, negative correlation (e.g. identical data with opposing signs). Below, Pearson correlation was calculated between each dataset as a function of temperature for XRD, PDF, and IR data using the python package Pandas.[4] The distinct transitions in color demonstrate the chemical transitions observed during the reaction.

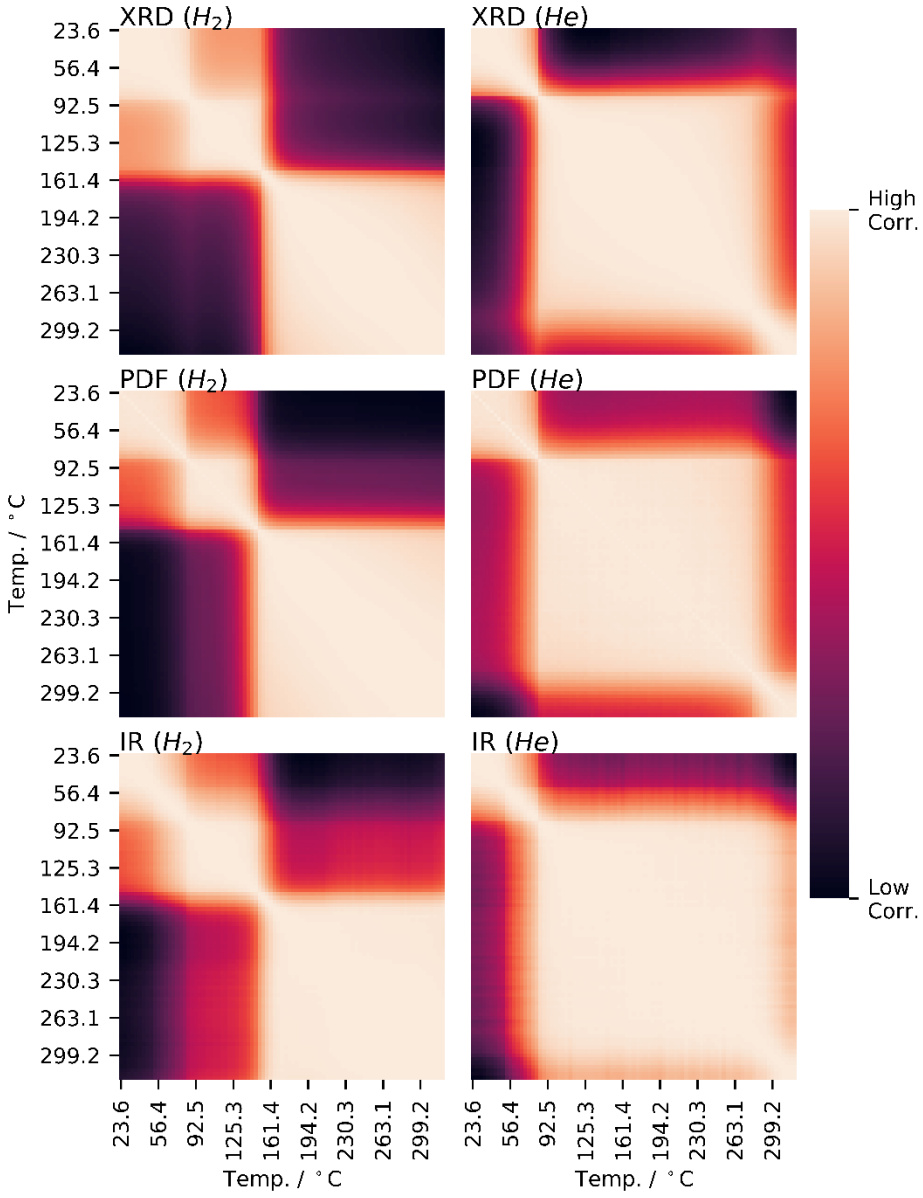

Figure S2. *Maps of Pearson correlation coefficient*

X-RAY SCATTERING ANALYSIS

X-ray scattering data measured as a function of temperature are shown in **Figure S3**.

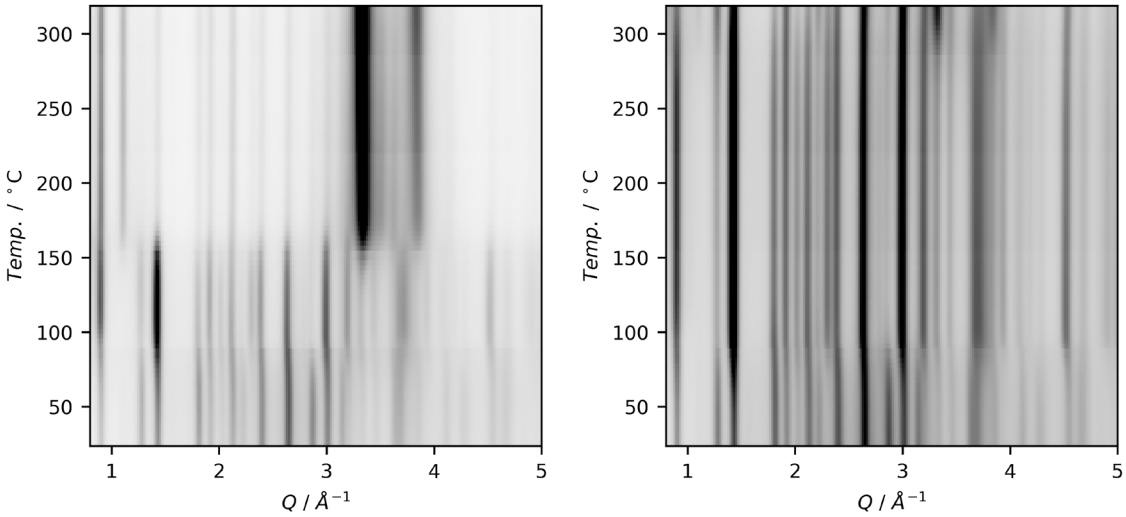

Figure S3. *Variable temperature X-ray diffraction data collected under reducing (left) and inert atmosphere (right).*

XRD data was analyzed in TOPAS[5] with lattice parameters and peak intensities estimated using Le Bail fits based on the reported structure of LTA. A split-pseudo-Voigt function ("PV_Left_Right" in TOPAS) was fit to the diffuse feature at low angle to quantify the scattering intensity. A 8-coefficients Chebyshev polynomial function was used to fit the background. The diffraction data for the initial Ag-exchanged LTA could be fit as a cubic phase (*Pm*-3*m*) with refined lattice parameter a = 12.20 Å. This is consistent with the known structure for LTA. (Note: for simplicity we applied the disordered Al/Si model with lattice a = 12.20 Å rather than the Al/Si ordered model with lattice a = 24.4 Å).

Structure envelopes (SEs) were calculated at selected temperatures, based on the measured peak intensities, as described previously.[6] The structure envelope is a low-resolution surface that divides regions of high electron density (occupied by the framework and Ag guests) and regions of low electron density (reflecting unoccupied pore space). The envelope analysis used 12 reflections ({001} to {213}). Difference envelope density (DED) maps reflecting the redistribution of electron density within the pores were obtained by subtracting the SE obtained under different conditions. As the X-ray scattering intensity data were normalized based on the high Q-region, no further normalizations were applied as part of the DED analysis.

In a reducing atmosphere: The lattice dimension of the LTA initially contracts slightly (<0.07 %) with heating, but then expands sharply (by 0.56% to a = 12.27 Å) during the first transition. With further heating, the lattice contracts slightly (<0.1%), before contracting sharply during the second transition, approaching the original dimension. With heating beyond the second transition, the lattice expands slightly.

A small angle scattering feature appears during the first transition. This diffuse X-ray scattering intensity appears at lower angles than the first diffraction peak of the LTA framework (Q < 0.4 Å^{-1}). Such small angle scattering features reflect nanoscale structure within the system and is a signature of Ag cluster or nanoparticle formation. The intensity of small-angle scattering is correlated to the concentration of

nanoscale features. The *Q*-value at which this feature is observed reflects the size of the nanoscale features, according to the relation $d = 2\pi/Q$, and will be centered at lower angle for large nanoparticles compared to small clusters. However, as the small angle scattering feature is partially obscured by the X-ray beam stop at low angle, changes in the position of the feature cannot be directly quantified. Instead, increase in the particle size is indirectly reflected in a reduction in the intensity in the accessible low angle scattering.

The intensity of the small angle scattering feature that reflects Ag clusters and nanoparticles formation increases during the second transition, then decreases with further heating. A new series of diffraction peaks, consistent with polycrystalline face-centered cubic (FCC) Ag^0 metal, emerge at the onset of the second transition. The diffraction peaks are broad, which indicates disorder and/or limited particle size of the Ag^0. Discontinuities in the intensity of the Ag^0 peaks coincide with the collection of detector dark images; these do not reflect real changes in the Ag^0 population.

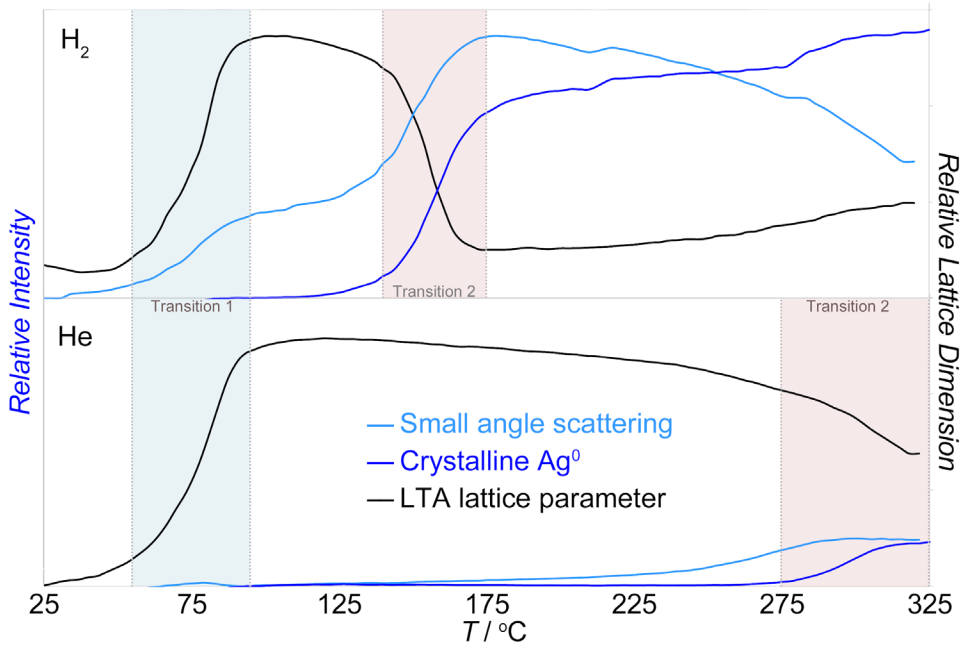

Figure S4. The changes in the LTA lattice dimensions and intensity of the small angle scattering feature and Ag^0 diffraction peaks in reducing (top) and inert (bottom) atmospheres. The transition regions are shaded**.**

In an inert atmosphere: The trends in the LTA lattice dimensions mirror those seen under reducing atmosphere, albeit with the second transition being shifted to higher temperature and being incomplete within the temperature range evaluated. In contrast to observations under reducing atmosphere, the small angle scattering intensity is not observed during in the first transition, appearing only in the second transition. The growth of the small angle scattering feature is observed at slightly lower temperature (by ca. 50 °C) than the appearance and growth of diffraction peaks from an FCC Ag^0 phase.

X-RAY PDF ANALYSIS

X-ray PDFs were extracted with XPDFsuite[7] (Q_{max} = 17.8 Å^{-1}) subtracting the background contribution of the sample environment cell. The PDFs contain contributions from all atom-atom pairs within the sample, including those from the zeolite lattice and the supported Ag material. The complete temperature-dependent PDFs and selected PDFs are shown in **Figure S5** and **Figure S6**.

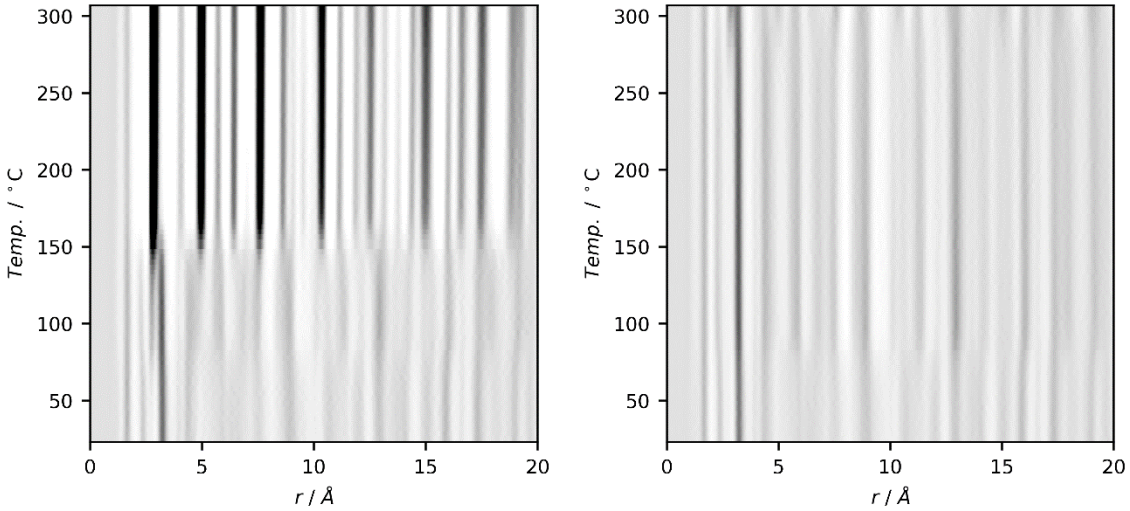

Figure S5. *Variable temperature PDF data collected under reducing (left) and inert atmosphere (right).*

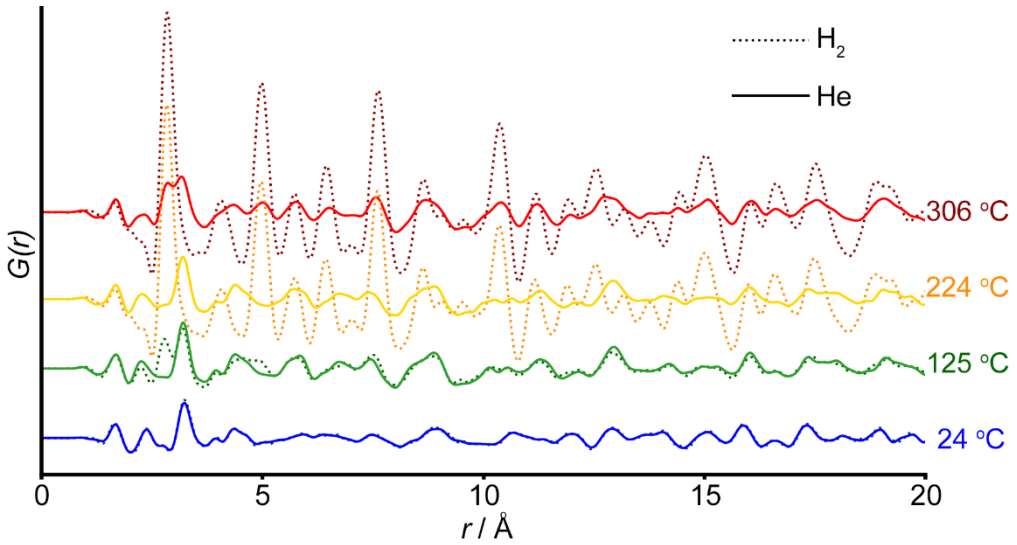

Figure S6. *Selected temperature PDF data collected under reducing and inert atmosphere.*

The PDF for the initial AgA includes atom-atom distances associated with the aluminosilicate lattice, such as the Si/Al-O bond at 1.6 Å. Atomic correlations involving the more strongly scattering Ag atoms, dominate the data. Peaks at 2.4 Å and 3.4 Å correspond to Ag-O (water and framework) and Ag···Si/Al distances, respectively. Structural models were refined against the PDF data within PDFgui[8] (**Figure S7**). The PDF of AgA at room temperature was fit by the reported crystallographic model of LTA, with lattice parameter a = 12.22 Å. The largest misfit in the data, between 5.5-6.3 Å, is most likely due to water within the pores that is not included in the model. Changes in critical features in the PDF data during heating in reducing and inert atmospheres are described in detail below.

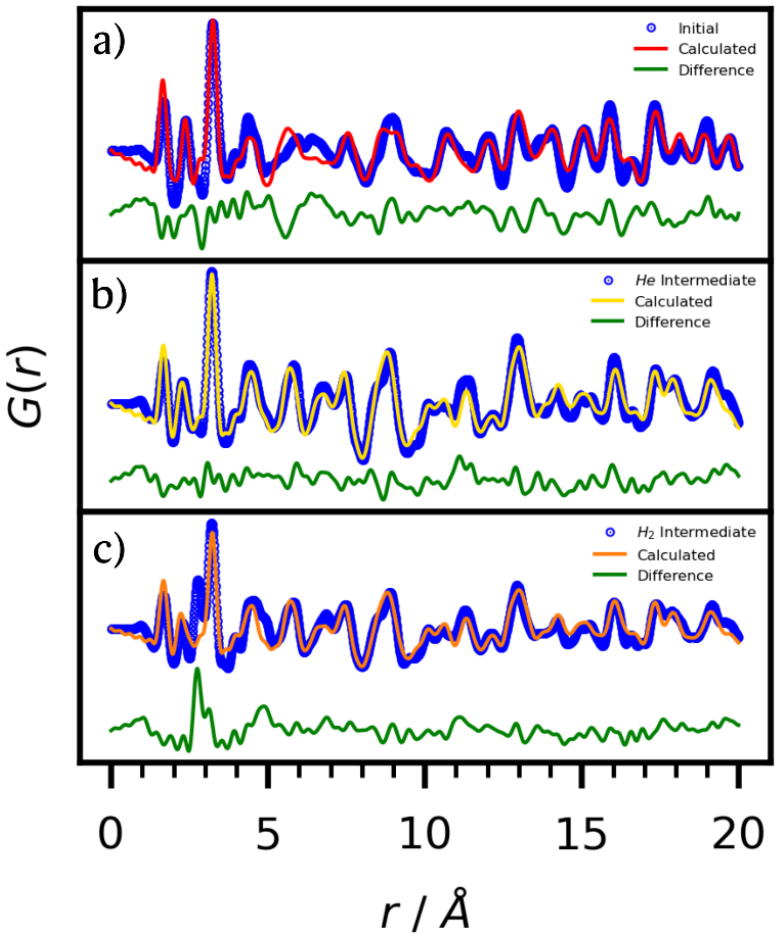

Figure S7*. Fits of to selected PDF data for a) the initial sample collected at 24 °C; b) the intermediate state at 125 °C under inert atmosphere; c) the intermediate state at 125 °C under H_2 flow. In c) the residual to the fit reflects the contribution from the Ag clusters*

In the reducing atmosphere: The PDF data show few discernable changes below the first transition.

A structural transformation is observed during the first transition, with changes to the PDFs that propagate to high *r*. This indicates an ordered rearrangement of atoms in the LTA crystal structure. The changes in local structural are characterized by shift of the peak at 2.4 Å to shorter distance (with a slight intensity reduction). This reflects a contraction of Ag^{+}···O distances and loss of coordinated water (supported by DRIFTS, vide infra). The peak at 3.4 Å, corresponding to the Ag···Al/Si distance, sharpens

and shifts to shorter distance, reflecting a narrower distribution of these correlations. A new peak is observed at *ca.* 2.78 Å, characteristic of Ag-Ag bonds in reduced Ag^0.

The PDFs in the intermediate state, following the first transition, were fitted with an LTA model having an expanded lattice parameter (a = 12.27 Å). The most significant structural change is displacement of Ag^+ cations that are centered over the 6-ring at (x,x,x) where x ~0.2. This corresponds to a shift from x = 0.218 in the initial Ag-exchanged LTA, to x = 0.203 in the intermediate state. The Ag^+ cations, which initially protrude from the plane of the 6-ring O atoms by 0.55 Å, shift into the 6-ring plane (see **Figure 4**). The $Ag^+\cdots O$ distance for Ag that is trigonally coordinated by the 6-ring contracts from 2.34 Å to 2.27 Å. There is an accompanying relaxation of the surrounding zeolite framework.

Features associated with small Ag^0 species were evident in the residual to the fit of the intermediate LTA model, at 2.78 Å, 3.10 Å and 3.85 Å (**Figure S7**). These are only evident at short distance (<6 Å), indicating that the Ag^0 species exist as sub-nanometer clusters. The low intensity of the features from these Ag^0 clusters, compared to the LTA phase, indicate that these are present at a low concentration.

Strong, sharp peaks consistent with large FCC Ag^0 nanoparticles emerge during the second transition. These are characterized by peaks at 2.86 Å, 4.06 Å and 4.99 Å, which correspond to the neighbor, next-nearest neighbor and second-nearest neighbor Ag-Ag distances, respectively, with higher-order neighbor distances observed to high r. Refinement of an FCC structural model against the data indicate that these have an average particle size of ca. 4 nm. These strongly scattering Ag nanoparticles dominate the PDF data following the second transition, making it difficult to reliably model contribution from the LTA, although the residual to the fit includes unmodeled features including the final LTA zeolite state. The contribution from the FCC Ag^0 nanoparticles increases intensity with continued heating beyond the transition reflecting an increase in their population.

Fits to the PDF data at selected temperatures suggest that the observed changes can be described by the change in the populations of different species: the initial, intermediate, and final LTA, and the Ag^0 clusters and nanoparticles (**Figure S8**). That the evolution in the PDF data can be described by a linear combination of discrete species, indicates that the transitions between different states are first order.

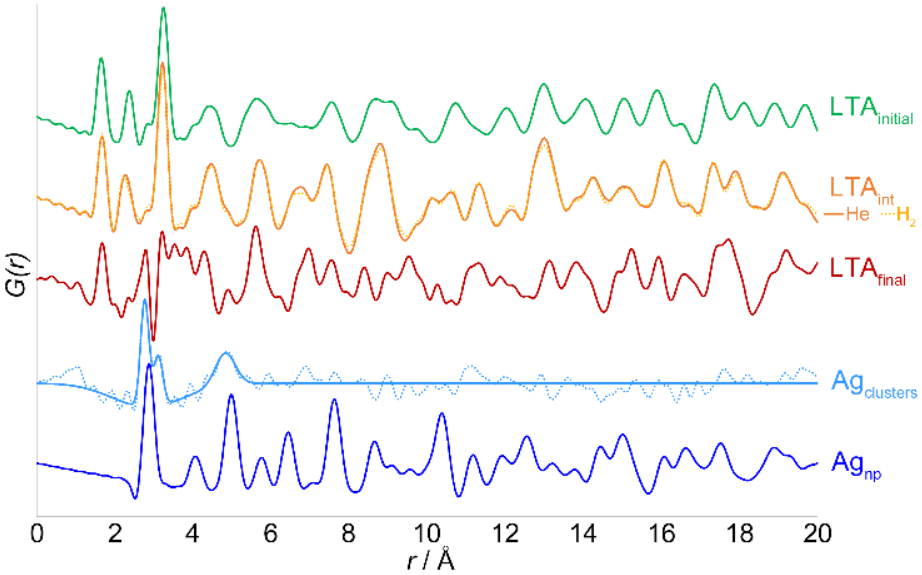

Figure S8. *Component PDFs used in a linear combination fit to the data. These were calculated based on refined structural models ($LTA_{initial}$, LTA_{int}, Ag_{np}) and derived from residuals to fits (LTA_{final}, $Ag_{clusters}$).*

A linear combination analysis (LCA) of the temperature-dependent PDF data, using the PDFs for individual components, was applied to quantify how the population of the distinct species evolve during heating (**Figure S9**). The specific components used for the analysis included the modelled PDFs for the initial LTA phase, the intermediate LTA phase, the 4 nm Ag^0 nanoparticles and the residuals to the PDF fits corresponding to the Ag^0 clusters and final LTA (here, the residual to the Ag^0 fit at high temperature).

The LCA fitting shows that the transformation between the initial and intermediate, and intermediate and final LTA states occur during the first and second transitions, respectively. The population of small Ag clusters emerges during the first transition. The population of the small Ag clusters initially grows at the onset of the second transition, then decreases with heating beyond the transition. The large Ag nanoparticle population emerges during the second transition and continues to increase in population, with heating beyond the transition, as the Ag cluster population decreases.

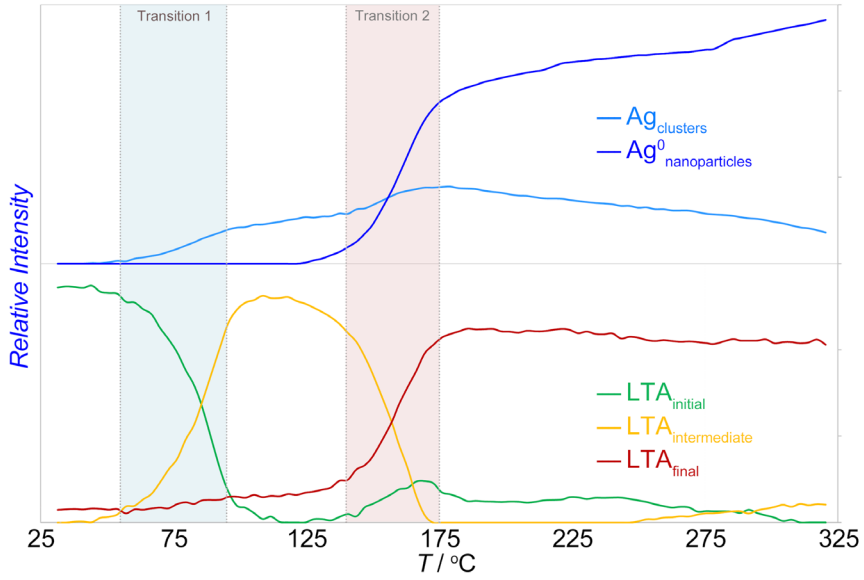

Figure S9. *The relative abundance of components during heating under reducing atmosphere from an LCA fitting to the PDF data. The different states of the LTA (bottom) support and Ag aggregates (top) are shown in separate panels.*

In the inert atmosphere: The transformations of the LTA lattice in the inert atmosphere are comparable to those seen under reducing atmosphere, albeit with the second transition being shifted to higher temperature and being incomplete within the temperature range evaluated. The intermediate AgA phase described under reducing atmosphere, with Ag^{+} cations shifted into the plane of the 6-ring, is observed. In contrast to observations made under the reducing atmosphere, the formation of the intermediate LTA state is not accompanied by the formation of a second phase of Ag^{0} clusters. Instead, small Ag^{0} clusters are apparent at the onset of the second transition, preceding the formation of features characteristic of FCC Ag^{0} nanoparticles.

The weightings from the LCA analysis (**Figure S10**), using the same PDF components as used under reducing atmosphere, reveal trends in species populations that were not directly apparent from inspection of the temperature-dependent PDFs. Notably, the same component phases are observed in the inert atmosphere as in the reducing atmosphere, however, these are formed at different temperatures and with different relative abundance. An increase in the Ag cluster population precedes the Ag nanoparticle formation.

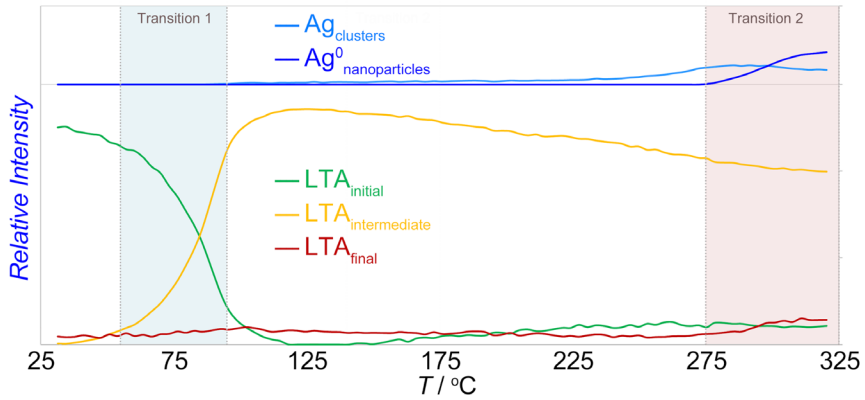

Figure S10. *The relative abundance of components during heating under inert atmosphere from a LCA fitting to the PDF data. The different states of the LTA (bottom) support and Ag aggregates (top) are shown in separate panels. The data are shown on the same scale as* ***Figure S7****.*

DRIFTS ANALYSIS

The baseline subtracted temperature dependent DRIFTS spectra are shown in **Figure S11**. The vibrational modes associated with different bands are summarized in **Table S1**.

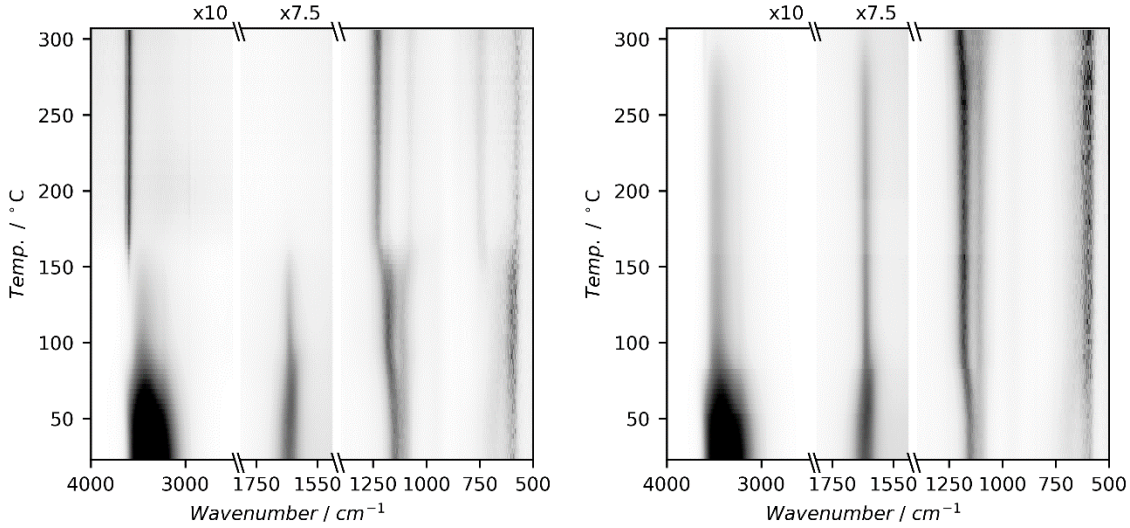

Figure S11. *Variable temperature DRIFTS data collected under reducing (left) and inert atmospheres (right).*

Table S1. DRIFTS observed peak assignments

Peak / cm^{-1}	**Assignment**
595	Ring blocks[9]
750	T-O-T symmetric stretch[9]
1080–1240	T-O-T/O-T-O asymmetric stretch[9]
1640	Molecular H_2O (free/weakly bound to Ag^+ cations and bound to Br ønsted acid sites)[10–11]
3200	Acidic OH group[12]
3400	Molecular H_2O (free/weakly bound and bound to aluminosilicate lattice)[11]
3570, 3605, 3640	Si-OH[11–13]
3680	Al-OH group[14–15]
5150	Molecular H_2O (free/weakly bound, combined bending and stretching)[10–12]

The intensity and position of DRIFTS features were quantified within Fityk.[16] Key features observed in the DRIFTS spectra include the OH stretching and H_2O bending modes from confined and weakly-bound H_2O, surface OH groups (i.e. Brønsted acid sites) and the T-O bonds within the LTA framework itself (see Figure 9). The bands were tentatively identified with the aid of previous assignments[21-26] resolving ambiguities by correlating the changes in the Ag species and zeolite distortions from the X-ray data. DRIFTS spectra for the initial AgA, contains peaks associated with molecular water at 1640 cm^{-1} (H_2O bending mode), 3000-3700 cm^{-1} (OH stretching mode), and 5207 cm^{-1} (combination H_2O bending + OH stretching mode). The broad feature, associated with OH-stretching modes (3000-3700 cm^{-1}), is characteristic of hydrogen-bonding interactions, with distinct bands initially centered at 3400 and 3250 cm^{-1} due to asymmetric and symmetric stretches respectively. OH-stretching bands from surface acid sites would also have peaks in this range (ca. 3580-3680 cm^{-1}),[21-25] however these are not present in the initial system. Well-defined bands between 1050 and 1250 cm^{-1} are associated with vibrations within the aluminosilicate lattice, specifically asymmetric O-T-O and T-O-T stretching modes. In the initial AgA, the strongest band in this range is observed at 1140 cm^{-1} (O-T-O internal asymmetric stretch) with a second band at 1090 cm^{-1}.

A comparison of the temperature-dependent DRIFTS spectra at selected temperatures in reducing and inert atmosphere is shown in **Figure S12**. During heating, the intensity of bands associated with the original H_2O/OH modes progressively disappear while new bands emerge. The changes in peak intensities effectively track the changes in concentration of distinct sites within the pores (H_2O) and on the surface of the zeolite (OH) during dehydration and Ag reduction. Shifts in the energy of bands, predominately T-O framework stretches, reflect a change in the stretching frequency and strength of those bonds due to changes in the local environment. An increase in the spectral "baseline" reflects a reduction in the sample reflectivity (i.e. a darkening or color change) owing to the formation of Ag aggregates (nanoparticles and clusters).

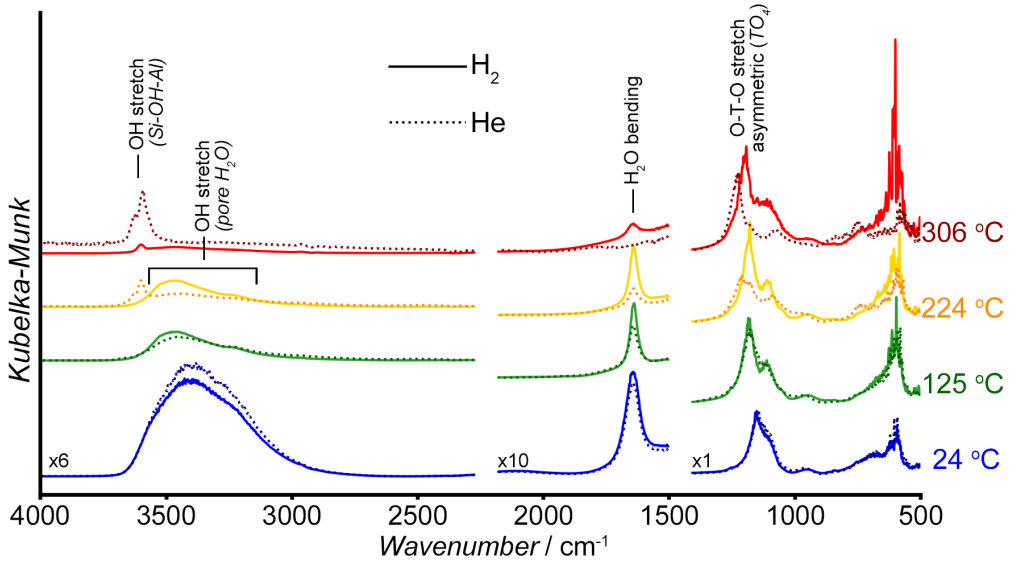

Figure 12 *Selected temperature-dependent DRIFTS data under reducing (dashed) and inert (continuous) atmospheres.*

In reducing atmosphere: Upon heating in reducing atmosphere, distinct changes to the DRIFTS features are observed (**Figure S13**). The sharp peak at 1640 cm^{-1} (H_2O bending), initially shifts to lower wavenumber (1630 cm^{-1}) and slightly increases intensity, but rapidly reduces to half the original intensity and returns to the original wavenumber during the first transition. With further heating, the intensity continues to reduce before being eliminated during the second transition. The intensity reflects the H_2O within the lattice. The small peak at 5250 cm^{-1} (H_2O combined bending-stretching), which reflects confined, unbound water progressively loses intensity during heating and is eliminated following the first transition. The broad feature between 3000-3700 cm^{-1} (OH stretching), progressively reduces intensity with heating, with a four-fold decrease in the original intensity during the first transition whereupon the broad band at 3400 cm^{-1} shifts to higher wavenumbers. This feature is eliminated following the second transition. A sharp peak at 3680 cm^{-1}, characteristic of acidic OH groups[25] (Si-OH-Al), forms during the first transition. The sharpness of this feature suggests that the acidic OH does not participate in hydrogen-bonding. The feature at 3680 cm^{-1} gradually reduces in intensity and is eliminated before the onset of the second transition. Two sharp peaks at 3640 cm^{-1} and 3600 cm^{-1}, also associated with acidic OH groups (Si-OH-Al), appear during the second transition. The baseline of the spectra increases as the sample reflectivity decreases, owing to formation of Ag aggregates. The changes in baseline were quantified based on the average intensity at ca. 5500 cm^{-1}, where no stretching/bending modes are evident. There is a slight increase in baseline during the first transition and a large increase in the baseline during the second transition.

Well-defined peaks at 1050 and 1250 cm^{-1}, which are associated with vibrations of the aluminosilicate framework, shift to higher wavenumber during the first transition to 1180 and 1110 cm^{-1}, respectively. During the second transition, band at 1180 cm^{-1} again blue shifts to 1225 cm^{-1}, while the peak at 1110 cm^{-1} red shifts to 1070 cm^{-1}.

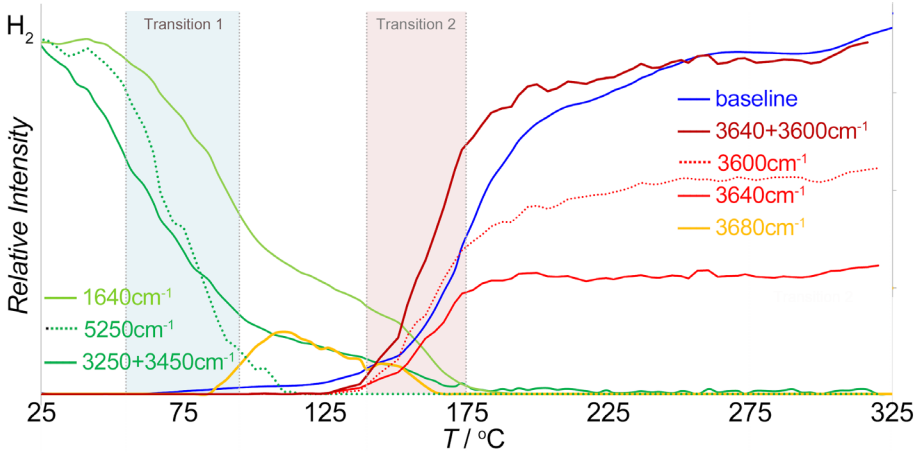

Figure S13. *The relative intensity of features in the IR data under reducing atmosphere. The intensity of the 3680 cm^{-1} peak is multiplied by a factor of 10 for clarity.*

In the inert atmosphere: Upon heating in inert atmosphere a series of changes to the DRIFTS features are evident (**Figure S14**). The initial bands associated molecular water - H_2O bending (1640 cm^{-1}), OH stretches (3000-3700 cm^{-1}), and combined bending-stretching mode (5250 cm^{-1}) - follow the same trends observed in reducing atmosphere, however with second transition shifted to higher temperature. The sharp feature at 3680 cm^{-1}, due to acidic OH groups, that was seen between the first and second transition under reducing atmosphere, is not evident in the inert atmosphere. A small peak emerges at ca. 3600

cm^{-1} during the second transition that can be attributed to acidic OH groups. In contrast to observations under reducing atmosphere, the baseline does not increase during the first transition, but only increases during the second transition.

The well-defined bands between 1050 and 1250 cm^{-1}, that are associated with vibrations of the aluminosilicate framework, show the same shifts in energy as seen during the first and second transitions under reducing atmosphere.

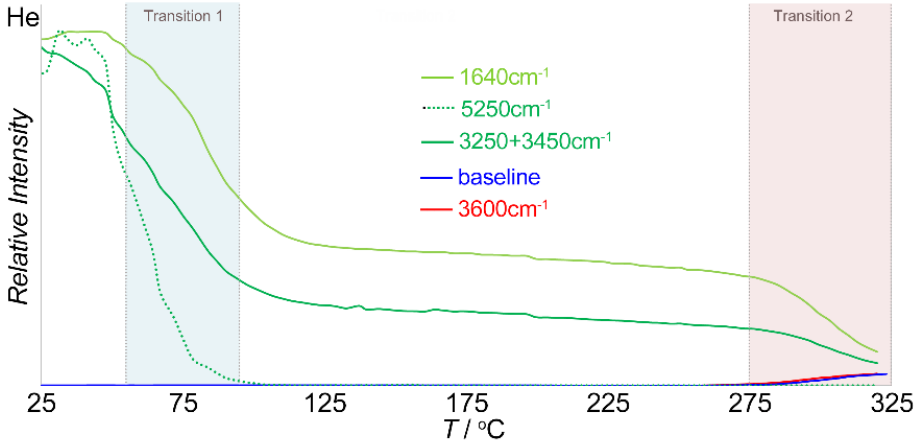

Figure S14. *The relative intensity of features in the IR data under reducing atmosphere.*

Peaks associated with O-T-O/T-O-T vibrations are observed at 595 cm^{-1} (ring block vibrations), 750 cm^{-1} (T-O-T symmetric stretch), and between 1080 cm^{-1} and 1240 cm^{-1} (T-O-T/O-T-O asymmetric stretches). The energy of these bands shift during the transitions (**Figure S15**). In reducing atmosphere, the asymmetric T-O stretch at 1150 cm^{-1} blueshifts to a plateau of 1180 cm^{-1} at 80 °C and then increases between 135 °C and 180 °C to another plateau of 1230 cm^{-1}. Similarly, between 145 °C and 180 °C, the peak at 1120 cm^{-1} both reduces intensity and shifts to 1080 cm^{-1}. Increase in temperature above 145 °C, leads to the presence of a peak at T-O-T symmetric stretch at 750 cm^{-1}. In inert atmosphere, the asymmetric T-O stretch at 1150 cm^{-1} blueshifts to a plateau of 1180 cm^{-1} at 80 °C and remains in that position for the remainder of the reaction. Similarly, the peak at 1120 cm^{-1} redshifts to 1105 cm^{-1}. Above 260 °C, a T-O-T symmetric stretch peak is observed at 700 cm^{-1}.

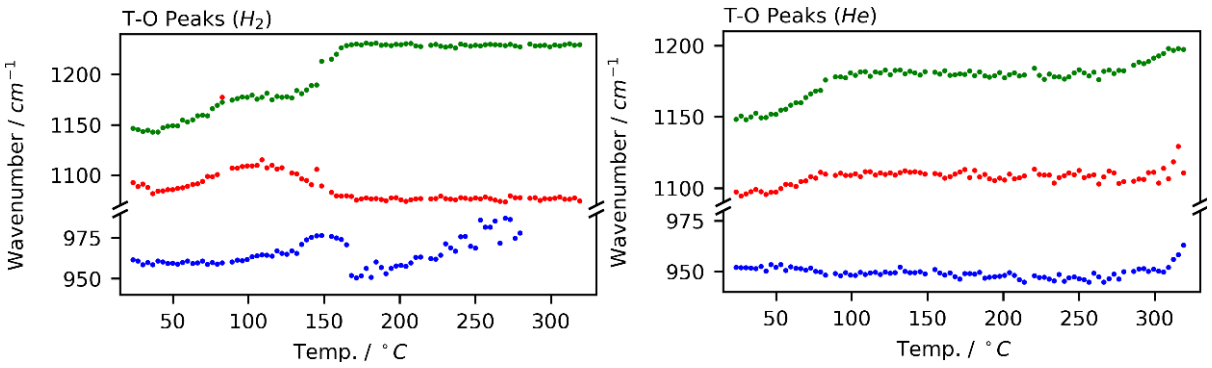

Figure S15. *Variable temperature trends in T-O peak positions in DRIFTS data collected under reducing (left) and inert atmospheres (right).*

MULTI-MODAL NON-NEGATIVE MATRIX FACTORIZATION

Correlating multimodal data using NMF. Values derived from the PDF, XRD and DRIFTS analyses were normalized between 0 and 1 and assembled into a matrix containing columns of parameters that vary during the Ag nanoparticle formation: 5 parameters from the PDF analyses (the weightings of 5 components from a linear combination analysis); 3 parameters from the XRD analysis (*a*, intensity of a Ag^0 peak, and the area of the small-angle scattering feature); and parameters from the DRIFTS (baseline and water/hydroxyl group peaks, 11 parameters for reducing atmosphere, 9 parameters for inert atmosphere). The NMF analysis was implemented using the SciPy python package.[17]

REFERENCES

1. Beyer, K. A.; Zhao, H. Y.; Borkiewicz, O. J.; Newton, M. A.; Chupas, P. J.; Chapman, K. W., Simultaneous diffuse reflection infrared spectroscopy and X-ray pair distribution function measurements. *J. Appl. Crystallogr.* **2014,** *47*, 95−101.
2. Chupas, P. J.; Chapman, K. W.; Lee, P. L., Applications of an amorphous silicon-based area detector for high-resolution, high-sensitivity and fast time-resolved pair distribution function measurements. *J. Appl. Crystallogr.* **2007,** *40*, 463-470.
3. Hammersley, A., FIT2D: a multi-purpose data reduction, analysis and visualization program. *J. Appl. Crystallogr.* **2016,** *49* (2), 646-652.
4. McKinney, W. In *Data Structures for Statistical Computing in Python*, 2010.
5. Coelho, A., TOPAS and TOPAS-Academic: an optimization program integrating computer algebra and crystallographic objects written in C++. *J. Appl. Crystallogr.* **2018,** *51* (1), 210-218.
6. Yakovenko, A. A.; Wei, Z.; Wriedt, M.; Li, J.-R.; Halder, G. J.; Zhou, H.-C., Study of Guest Molecules in Metal–Organic Frameworks by Powder X-ray Diffraction: Analysis of Difference Envelope Density. *Cryst. Growth Des.* **2014,** *14* (11), 5397-5407.
7. Yang, X.; Juhas, P.; Farrow, C. L.; Billinge, S. J. L., xPDFsuite: an end-to-end software solution for high throughput pair distribution function transformation, visualization and analysis. **2014**.
8. Farrow, C. L.; Juhas, P.; Liu, J. W.; Bryndin, D.; Bozin, E. S.; Bloch, J.; Proffen, T.; Billinge, S. J. L., PDFfit2 and PDFgui: computer programs for studying nanostructure in crystals. *J. Phys.: Condens. Matter* **2007,** *19* (33).
9. Bueno-Pérez, R.; Calero, S.; Dubbeldam, D.; Ania, C. O.; Parra, J. B.; Zaderenko, A. P.; Merkling, P. J., Zeolite Force Fields and Experimental Siliceous Frameworks in a Comparative Infrared Study. *J. Phys. Chem. C* **2012,** *116* (49), 25797-25805.
10. Davis, K. M.; Tomozawa, M., An infrared spectroscopic study of water-related species in silica glasses. *J. Non-Cryst. Solids* **1996,** *201* (3), 177−198.
11. Baumann, J.; Beer, R.; Calzaferri, G.; Waldeck, B., Infrared transmission spectroscopy of silver zeolite A. *J. Phys. Chem.* **1989,** *93* (6), 2292-2302.
12. Zholobenko, V. L.; Kustov, L. M.; Borovkov, V. Y.; Kazansky, V. B., A new type of acidic hydroxyl groups in ZSM-5 zeolite and in mordenite according to diffuse reflectance i.r. spectroscopy. *Zeolites* **1988,** *8* (3), 175−178.
13. Marie, O.; Massiani, P.; Thibault-Starzyk, F., Infrared Evidence of a Third Brønsted Site in Mordenites. *J. Phys. Chem. B* **2004,** *108* (16), 5073-5081.
14. Kloprogge, J. T.; Frost, R. L., Raman and infrared spectroscopic investigation of the neutralisation of aluminium in the presence of monomeric orthosilicic acid. *Spectrochimica Acta Part A: Molecular and Biomolecular Spectroscopy* **1999,** *55* (7), 1359−1369.

15. Kloprogge, J. T.; Ruan, H.; Frost, R. L., Near-infrared spectroscopic study of [AlO4Al12(OH)23(H2O)12]7+-O-Si(OH)3 nitrate crystals formed by forced hydrolysis of Al3+ in the presence of TEOS. *Spectrochimica acta. Part A, Molecular and biomolecular spectroscopy* **2000,** *56a* (12), 2405−11.
16. Wojdyr, M., Fityk: a general-purpose peak fitting program. *J. Appl. Crystallogr.* **2010,** *43* (5 Part 1), 1126−1128.
17. Virtanen, P.; Gommers, R.; Oliphant, T. E.; Haberland, M.; Reddy, T.; Cournapeau, D.; Burovski, E.; Peterson, P.; Weckesser, W.; Bright, J.; van der Walt, S. J.; Brett, M.; Wilson, J.; Millman, K. J.; Mayorov, N.; Nelson, A. R. J.; Jones, E.; Kern, R.; Larson, E.; Carey, C. J.; Polat, İ.; Feng, Y.; Moore, E. W.; VanderPlas, J.; Laxalde, D.; Perktold, J.; Cimrman, R.; Henriksen, I.; Quintero, E. A.; Harris, C. R.; Archibald, A. M.; Ribeiro, A. H.; Pedregosa, F.; van Mulbregt, P.; Vijaykumar, A.; Bardelli, A. P.; Rothberg, A.; Hilboll, A.; Kloeckner, A.; Scopatz, A.; Lee, A.; Rokem, A.; Woods, C. N.; Fulton, C.; Masson, C.; Häggström, C.; Fitzgerald, C.; Nicholson, D. A.; Hagen, D. R.; Pasechnik, D. V.; Olivetti, E.; Martin, E.; Wieser, E.; Silva, F.; Lenders, F.; Wilhelm, F.; Young, G.; Price, G. A.; Ingold, G.-L.; Allen, G. E.; Lee, G. R.; Audren, H.; Probst, I.; Dietrich, J. P.; Silterra, J.; Webber, J. T.; Slavič, J.; Nothman, J.; Buchner, J.; Kulick, J.; Schönberger, J. L.; de Miranda Cardoso, J. V.; Reimer, J.; Harrington, J.; Rodríguez, J. L. C.; Nunez-Iglesias, J.; Kuczynski, J.; Tritz, K.; Thoma, M.; Newville, M.; Kümmerer, M.; Bolingbroke, M.; Tartre, M.; Pak, M.; Smith, N. J.; Nowaczyk, N.; Shebanov, N.; Pavlyk, O.; Brodtkorb, P. A.; Lee, P.; McGibbon, R. T.; Feldbauer, R.; Lewis, S.; Tygier, S.; Sievert, S.; Vigna, S.; Peterson, S.; More, S.; Pudlik, T.; Oshima, T.; Pingel, T. J.; Robitaille, T. P.; Spura, T.; Jones, T. R.; Cera, T.; Leslie, T.; Zito, T.; Krauss, T.; Upadhyay, U.; Halchenko, Y. O.; Vázquez-Baeza, Y.; SciPy, C., SciPy 1.0: fundamental algorithms for scientific computing in Python. *Nature Methods* **2020,** *17* (3), 261-272.